

# Moisture Vertical Structure and Tropical Deep Convection

Submitted to the Journal of the Atmospheric Sciences,

April 2, 2008

Christopher E. Holloway \*

Department of Atmospheric and Oceanic Sciences,

University of California, Los Angeles, Los Angeles, California

J. David Neelin

Department of Atmospheric and Oceanic Sciences

and Institute of Geophysics and Planetary Physics,

University of California, Los Angeles, Los Angeles, California

---

\* *Corresponding author address:* Christopher E. Holloway, Department of Atmospheric and Oceanic Sciences, University of California, Los Angeles, 405 Hilgard Ave., Los Angeles, CA 90095-1565.  
E-mail: chollow@ucla.edu

## Abstract

The vertical structure of the relationship between water vapor and precipitation is analyzed in five years of radiosonde and precipitation gauge data from the Nauru Atmospheric Radiation Measurement (ARM) site. The first vertical principal component of specific humidity is very highly correlated with column water vapor (CWV) and has a maximum of both total and fractional variance captured in the lower free troposphere (around 800 hPa). Moisture profiles conditionally averaged on precipitation show a strong association between rainfall and moisture variability in the free troposphere, and little boundary layer variability. A sharp pick-up in precipitation occurs near a critical value of CWV, confirming satellite-based studies. A lag-lead analysis suggests it is unlikely that the increase in water vapor is just a result of the falling precipitation. To investigate mechanisms for the CWV/precipitation relationship, entraining plume buoyancy is examined in sonde data and simplified cases. Higher CWV results in progressively greater plume buoyancies for several mixing schemes, notably upper-tropospheric buoyancy that can yield deep convection. All other things equal, higher values of lower-tropospheric humidity, via entrainment, play a major role in this buoyancy increase. A small but significant increase in subcloud layer moisture (and thus equivalent potential temperature) with increasing CWV also contributes to buoyancy. Entrainment based on mass flux increase through a deep lower-tropospheric layer yields a relatively even weighting for the impact on mid-tropospheric buoyancy of all lower levels, explaining the association of CWV and buoyancy available for deep convection.

# 1. Introduction

A number of studies indicate that moist convection is sensitive to free-tropospheric water vapor, including observational analyses (Parsons et al. 2000; Bretherton et al. 2004) and studies using cloud-system resolving models (Tompkins 2001b; Grabowski 2003; Derbyshire et al. 2004). This dependence is apparently not well represented in global climate models (GCMs) (Derbyshire et al. 2004; Biasutti et al. 2006; Dai 2006)—but sensitivity has been shown in some cases (Zhang and Wang 2006, Richter and Neale 2008, manuscript submitted to *J. Climate*). Recent work also suggests that the inability of most GCMs to simulate multi-scale convective organization, including intraseasonal variability associated with the Madden-Julian Oscillation (MJO), may be due primarily to this lack of a positive feedback between free-tropospheric moisture and convection (Grabowski 2006).

Since precipitation processes in climate models are very sensitive to the method of convective parameterization (Slingo et al. 1996), it is of interest to investigate the relationship between tropospheric moisture and precipitation in observations and its representation in convective parameterizations. Regions where the trade winds flow into convection zones tend to exhibit sensitivity to changes associated with teleconnections and global warming, and they are also sites of disagreement in simulated precipitation among different models (Neelin et al. 2003, 2006). Inflow of drier tropospheric air is typical in these locations. The interaction between inflow across moisture gradients and the difficulty of convective parameterizations in simulating the sensitivity of convection to free-tropospheric moisture could play a role in the model discrepancies in these regions (Lintner and Neelin 2007).

A few recent studies have illustrated an empirical relationship between tropical column water vapor, CWV (scaled by some mea-

sure of free-tropospheric temperature, which does not change very much in the deep tropics) and precipitation, including a sharp pick-up of average precipitation at sufficiently high CWV (Bretherton et al. 2004; Peters and Neelin 2006). In the present study, we investigate the vertical structures of water vapor variability at Nauru Island in the western equatorial Pacific. One goal is to better understand the vertical distribution of the moisture variance associated with CWV, a metric easily available from satellite data. Another motivation is to investigate the main vertical structures of water vapor perturbations, providing insight for intermediate-complexity models which represent water vapor with one or a few vertical structures, such as the quasi-equilibrium tropical circulation model (QTCM; Neelin 1997; Neelin and Zeng 2000).

After characterizing the vertical structure of water vapor and its relationship to average precipitation and CWV in section 3, we turn to the effects of different environmental profiles of moisture on simple plume models of convection in section 4. Analysis in terms of an entraining plume (e.g., Raymond and Blyth 1992; Brown and Zhang 1997; Jensen and Del Genio 2006) is used to connect the increased buoyancy of entraining plumes in moist environments with the sharp pick-up of average precipitation at high CWV. We also investigate the role of subcloud layer moistening versus free-tropospheric moistening on entraining plume buoyancy. The sensitivity of the results to assumptions of mixing profiles and microphysics in section 5 provide insight into the challenges of incorporating environmental humidity in convective parameterizations.

## 2. Data

The Department of Energy’s Atmospheric Radiation Measurement (ARM) Program (Stokes and Schwartz 1994) maintains a climate observation site at Nauru Island (0.5°S, 166.9°E; Mather et al. 1998). We have an-

alyzed radiosonde temperature and moisture data and optical gauge surface precipitation from 1 April 2001 to 16 August 2006. The radiosonde data have been interpolated onto 5 hPa levels. The uncertainty of the Vaisala (RS80, RS90, and RS92) radiosondes is approximately  $0.5^{\circ}\text{C}$  for temperature and 5% for relative humidity, although in the upper troposphere (above 500 hPa) relative humidity uncertainties can be much larger (Westwater et al. 2003). The main observations occur twice a day, at 00z and 12z, with occasional sondes around 14z and 02z.

The precipitation rate is measured at 1-min intervals by an optical gauge with  $0.1\text{ mm hr}^{-1}$  resolution and  $0.1\text{ mm hr}^{-1}$  uncertainty. For comparison with the radiosondes, a 1-hr average rain rate has been computed, centered at the launch time of each radiosonde. Since the sonde takes about 45 minutes to rise through the troposphere, this averaging window should give a good characterization of the precipitation conditions in the airmass through which the sonde rises. Time averaging also helps reduce the precipitation measurement noise inherent in the use of a single gauge; averaging over many hourly events, as is done in the analyses of this study, further reduces this noise.

The sonde pressure, temperature, and humidity data have had a basic quality check at ARM, and have been further constrained to be within reasonable ranges; the lowest-altitude sonde data have also been checked for agreement with ARM surface data. In total, 3,491 sondes have been retained for the complete analysis (with 200 additional sondes containing acceptable data at some levels included in the water vapor variability analyses). The radiosonde versions analyzed in this study are not thought to have much dry bias, which characterized earlier Vaisala sonde versions (B. M. Lesht 2007, personal communication). The sonde total CWV values compare fairly well with 1-hr averages of microwave radiometer values, with a correlation coeffi-

cient of 0.92. A slight tendency for the sondes to be moister than the radiometer at high CWV likely occurs because the radiometer cannot operate during rainfall and may have difficulties when cloud water is large.

### 3. Characterizing the vertical structure of moisture

An important step in investigating the vertical structure of the transition to deep convection is characterizing the vertical structure of moisture variations as a whole. This endeavor is more complicated than the analogous problem for tropical temperature perturbation structures, which tend to follow reversible moist adiabats and are smoothed in the horizontal by gravity waves, at least in the free troposphere on large enough space and time scales (e.g., Xu and Emanuel 1989; Holloway and Neelin 2007). Water vapor has smaller spatial uniformity than temperature in the tropics, and is more locally influenced by evaporation, precipitation, and advection. Here we investigate the vertical variability of water vapor at Nauru and relate this to CWV, which in turn is related to precipitation.

#### *a. Effect of precipitation on moisture structure*

Profiles of specific humidity  $q$  conditionally averaged on precipitation (Fig. 1) reveal that it is mainly free-tropospheric moisture, rather than boundary layer moisture, which increases with increasing rainfall. The spread among the curves is larger than the maximum confidence interval, indicating that the separation of the mean specific humidity at many tropospheric levels by average precipitation is real. Note that the bins double in width with increasing precipitation and that most of the sondes fall into the first bin (see caption for bin counts), which is basically non-precipitating, so that  $q$  profile in that bin is actually fairly representative of the mean profile overall. In

the highest precipitation bin, there is actually a decrease in the subcloud layer moisture compared to the other bins, probably due to subsaturated downdrafts forming cold pools (see section 3e).

Figure 1 can be compared to analyses of monthly and daily specific humidity sondes conditionally averaged on precipitation in Bretherton et al. (2004, their figures 9 and 10a). While their monthly means from many long-term tropical radiosonde stations do not show much difference between spread at free-tropospheric levels and spread in the boundary layer, their two months of daily Tropical Rainfall Measurement Mission (TRMM) Kwajalein Experiment (KWAJEX) sondes do show variability similar to that in these 5 years of ARM twice-daily data, although their values are a little lower. Concurrent work by Nuijens et al. (2008, manuscript in preparation) for trade cumulus conditions near Barbuda finds a similar relationship between lower-free-tropospheric humidity and precipitation.

*b. Leading vertical structure and relation to column water vapor*

Two recent studies have investigated a statistical link between CWV and precipitation using satellite data. Bretherton et al. (2004) show that, on daily and monthly scales, precipitation increases roughly exponentially with CWV. Peters and Neelin (2006) find that precipitation, conditionally averaged by CWV over many individual events, tends to increase slowly up to some critical value and then rapidly increase above that. This kind of relationship can be detected in these ARM data as well, as discussed below in section 3c. An important question, however, concerns how the variance of CWV is distributed over different vertical levels.

Figure 2a shows the results of principal component analyses (using the covariance method) performed on each level of  $q$  from 1000–200 hPa for all available sondes and for a much smaller “high precipitation” subset of

sondes that occur within  $\pm 3$  hours of 1-hr precipitation values greater than  $2.56 \text{ mm hr}^{-1}$  (red and blue lines, respectively). The solid lines show the variance explained by the first principal component (PC 1) for the two analyses, while the long-dashed lines show the total variance of  $q$  at each level. These principal components represent 53% and 49% of the total variance for all sondes and the high precipitation sondes, respectively. In both analyses, the second principal component represents a much smaller fraction of the variance, and is not well separated from the other higher principal components. The dotted red line shows total variance at each level of a hypothetical specific humidity field derived only from temperature and a fixed relative humidity profile (taken from the mean of all original sondes). This shows that observed changes in temperature alone, assuming constant relative humidity, could account for only a small amount of the total moisture variances. This is generally expected in the tropics for these short time scales, and appears to be particularly true at this western Pacific location.

The solid curve can be divided by the dashed curve in each case to get the fractional variance represented by PC 1 at each level, shown in Fig. 2b. The square roots of these profiles (the correlation coefficients between PC 1 and  $q$  at each level, not shown) line up fairly well with correlations between CWV and water vapor mixing ratio found for an average over soundings from many research vessel cruises in the tropics (Yoneyama 2003, their figure 5a).

The most striking feature of these figures is the large peak in the lower troposphere for both total variance and fractional variance represented by PC 1. It makes sense that variance decreases upwards in the upper troposphere, since increasingly colder temperatures limit the amount of water vapor that the air can hold, and therefore the variance of water vapor as well. Smaller total variance at boundary layer levels is in agreement with many pre-

vious studies suggesting that boundary layer  $q$  is tied fairly closely to SST, whereas free-tropospheric  $q$  can vary greatly due to processes such as dry air intrusions and advection from convective regions (e.g., Liu et al. 1991; Yoneyama 2003). However, the small fractional variances in the boundary layer shown in Fig. 2b reveal that the maximum shared variance (PC 1 in each case) is dominated by the lower troposphere even more than would be predicted based on a fixed fraction of the total variance.

Figure 2c shows the contributions to the CWV variance from the vertically-integrated boundary layer (surface–850 hPa) and free-tropospheric (850–200 hPa) water vapor. Even though the boundary layer contains a mean vertically-integrated contribution to column water of 27.5 mm, slightly higher than the corresponding value of 24.5 mm in the free troposphere, it is clear from the correlations and regressions (which add to one, since these two layers add up to give CWV) that a large majority of the total column variance is explained by the free-tropospheric layer.

Figure 2d confirms that, for each of these cases, the first principal component shown in Figure 2a,b is almost perfectly correlated with CWV, in agreement with Liu et al. (1991). Therefore, the solid curves in Fig. 2a represent the variance at each level explained by CWV, which as a whole represents approximately 50% of the total variance in each case as shown in the figure. Applying the above findings for PC 1, this means that free-tropospheric levels contribute the great majority of the total CWV variance, to an even greater extent than would be expected by simply taking a fixed fraction of the total variance at each level, and despite the slightly larger mean vertically-integrated moisture contained below 850 hPa. Not only do free-tropospheric levels have larger  $q$  variances than boundary layer levels, they also vary together to a much greater extent than they share variance with boundary layer levels (as shown by the high

PC 1 loadings in the lower free troposphere). This implies that, to a very good approximation, CWV could be represented by a free-tropospheric vertically-integrated  $q$  added to a mean boundary layer value (or even better, a boundary layer value that is a linear function of the free-tropospheric value).

*c. Free-tropospheric versus boundary layer vertically-integrated water vapor: relationship to moisture structure and precipitation*

To illustrate the vertical profiles of moisture associated with different amounts of column water, and specifically with the transition to high precipitation, we conditionally average sonde profiles on water vapor integrated over three different vertical layers. Figure 3a shows specific humidity profiles conditionally averaged on total CWV (the bins are equal-width except for the two outer bins, as shown on the color bar). Although there is some spread in the boundary layer, the largest spread occurs around 800 hPa, consistent with Fig. 2a.

For CWV bins below about 50 mm, the subcloud layer (below 950 hPa) is more vertically constant and more sharply distinguished from the troposphere, as expected for stable subsidence conditions. Much of the tropospheric variability in these bins is also consistent with subsidence altering air that had once been closer to saturation, with a typical maximum in the middle of the troposphere, causing the stretching at middle levels. Figure 3a also fits well with previous descriptions of dry intrusions in the free troposphere, which can suppress deep convection for over a week while shallow convection slowly moistens the lower troposphere (Numaguti et al. 1995; Mapes and Zuidema 1996; Brown and Zhang 1997; DeMott and Rutledge 1998; Parsons et al. 2000).

Much of the variability occurs at the lower end of the CWV range, as discussed above; this is not seen for the humidity profiles conditionally averaged on precipitation shown in

Fig. 1. This is expected because the lowest precipitation bin in that figure contains the vast majority of sondes, which probably include mostly sondes with middle and drier CWV values, as well as some higher values. This association of near-zero precipitation with the lower half of CWV bins is confirmed by Fig. 3b, which shows precipitation conditionally averaged on the same CWV bins as in Fig. 3a. There is clearly a sharp pick-up of precipitation above about 67 mm CWV. This jump is significant, as indicated by the vertical bars representing  $\pm 1$  standard error. The general increase in precipitation agrees with daily mean values in Bretherton et al. (2004), although their curves stop below 65 mm CWV. The sharp pick-up of precipitation roughly agrees with Peters and Neelin (2006) in both CWV value and shape, although the small number of sondes in the bins with highest CWV (illustrated by the inset in Fig. 3a) makes it impossible to confirm whether the curve follows a power law function as observed in that study.

When the specific humidity profiles and precipitation are conditioned on just the free-tropospheric column water (850-200 hPa, with bin edges chosen to correspond as much as possible to those for the total CWV), the results are similar to those found with the total CWV. This is expected, since section 3b showed that lower-free-tropospheric  $q$  variance dominates CWV variance. Indeed, Fig. 3c shows even less variance in the boundary layer, which of course follows from the use of a free-tropospheric layer for the conditional averaging. The precipitation averages in Fig. 3d actually seem to have an even smoother pick-up of similar shape to that in Fig. 3b.

Figures 3e,f confirm that the subcloud layer (up to 950 hPa) is much less related to CWV. Little of the free-tropospheric variability illustrated for CWV in Fig. 3a is captured in Fig. 3e. The precipitation averages in Fig. 3f perhaps suggest a slight, noisy increase

in precipitation with subcloud layer moisture, but the values are much smaller. This relationship has implications for intermediate-complexity models such as the QTCM. A single vertical degree of freedom in moisture indeed captures much of the effect on precipitation, but its variance is primarily in the free troposphere. Modeling can thus benefit from two degrees of freedom in the vertical (c.f. Neggers et al. 2007; Sobel and Neelin 2006) to allow the free troposphere to be separated from the boundary layer, which tends to be closely tied to surface conditions.

#### *d. Relative Humidity Structure*

A question which naturally follows from Figures 1–3 is the extent to which the higher values of specific humidity are approaching saturation. Figure 4a shows that, for the highest precipitation bins, the average relative humidity ranges from 85–90% in the lower and middle troposphere. The lowest precipitation bin, which contains the vast majority of sondes (and is therefore a much smoother curve) is at the lowest end in relative humidity. However, there is much more of a spread in relative humidity when profiles are conditionally averaged on CWV, as shown in Fig. 4b. The relative humidity is around 95% for the very highest bins from 900 hPa through about 600 hPa, and there is also a large amount of variability among the bins at these levels. Clearly, the specific humidity variability shown in Figure 3a corresponds to large changes in relative humidity, rather than changes in temperature at constant relative humidity.

#### *e. Precipitation Lag-Lead Analysis*

An important question regarding the association between CWV and precipitation is whether observations can supply an indication of causality. There are reasons to expect feedbacks in both directions. Convection can moisten the column via moisture convergence, detrainment and evaporation (although

on a larger scale convection is a net sink of moisture). A likely mechanism by which increased lower-tropospheric moisture could play a causal role in enhancing convection—by allowing entraining plumes to maintain higher buoyancy—is investigated in sections 4 and 5. Effects of CWV on buoyancy via entrainment (Raymond 2000; Tompkins 2001b; Grabowski 2003) appear to be quite important in Derbyshire et al. (2004) compared to other mechanisms involving downdrafts and cold pools (e.g., Raymond 1997; Tompkins 2001a), although these and radiative mechanisms (Mapes and Zuidema 1996) may also play a role.

A lag-lead analysis on precipitation versus CWV can help strengthen or weaken a causality argument. Figure 5 shows profiles of average specific humidity and relative humidity anomalies (taken as differences from the highly populated bin with precipitation less than  $0.0025 \text{ mm hr}^{-1}$ ) for precipitation above  $2.56 \text{ mm hr}^{-1}$  lagging and leading the radiosonde by up to three hours. The black curves are the same anomaly for no lag, and are placed in all figures for comparison purposes. In general, Figs. 5a,b show that  $q$  increases slightly in the upper troposphere above 500 hPa during and after precipitation, whereas below 750 hPa  $q$  tends to decrease after it rains and is rather constant or even slightly higher before rainfall. This pattern largely holds for the relative humidity profiles shown in Figs. 5c,d. Near the surface, temperatures cool on average after precipitation:  $q$  is lower than before precipitation while relative humidity is slightly higher. This is likely due to subsaturated downdrafts causing cold pools. Precipitation leading relative humidity in the upper troposphere and lagging relative humidity in the lower troposphere was also found in TRMM KWAJEX data by Sobel et al. (2004). The standard error bars for the  $q$  plots give an indication that the lag-lead curves are significantly different from the no-lag curve at most levels, although not neces-

sarily from each other. The relative humidity curves are still significantly different from the no-lag curve at many middle-tropospheric levels, but at upper and lower levels they are not as clearly separate.

This analysis casts doubt on the idea that increased precipitation is the cause of increased CWV, rather than vice versa, at least on these time scales. Following precipitation, there is a small increase in  $q$  above 500 hPa, where it does not have much effect on CWV. In the lower troposphere, there is, if anything, a decrease in  $q$  after the precipitation. On the other hand, this analysis also does not provide strong evidence for moisture at lower levels increasing greatly prior to precipitation and/or decreasing greatly after precipitation. The moisture at all precipitation lags at nearly all levels tends to be much higher than the moisture for nonprecipitating times, since all of the curves are much closer to each other than they are to zero. Indeed, a comparison with Fig. 2 suggests that the main mode of variance for  $q$  is captured by all of the curves in Figs. 5a,b, regardless of precipitation lag. In other words, within six hours centered around heavy precipitation the atmosphere has already been moistened to near-maximum levels. The smaller amount of variance for these higher precipitation times (Fig. 2a, blue lines) is also consistent with the differences between the various curves in Figs. 5a,b, which tend to be relatively small but take up a relatively deep layer.

A likely interpretation of these results is that high CWV tends to persist for relatively long times, increasing the chance of precipitation during those times. This is supported by an analysis of microwave radiometer and gauge data from Nauru showing that CWV has much higher characteristic autocorrelation times than precipitation or cloud water (Neelin et al. 2008). These findings also seem compatible with suggestions that much of the variance in water vapor in the tropics may be due to dry air intrusions from the midlatitudes or

subtropics that moisten relatively slowly, as mentioned in section 3c above.

## 4. Impact of tropospheric moisture on buoyancy: basics

### a. Moist stability profiles

Figure 6 shows  $\theta_e$  and  $\theta_{es}$  for all the bins shown in Fig. 3a above 50 mm CWV. (Since we are mainly interested in the changes that occur around and above the precipitation pickup, which occurs around 67 mm for these data, we have grouped all of the values below 50 mm into only two wide bins, which therefore have proportionately higher counts). An approximate measure (though one that does not account for the effect of condensate on virtual temperature) of parcel buoyancy and convective available potential energy (CAPE) is to draw a vertical line upwards from  $\theta_e$  at the parcel starting level. Where this line crosses the  $\theta_{es}$  curve is roughly the level of free convection (LFC) of the unmixed parcel; the area to the left of the vertical line and to the right of the  $\theta_{es}$  curve is roughly proportional to CAPE. It is clear that, for the highest CWV bins, there are potentially buoyant parcels starting from many lower-tropospheric levels (up to 800 hPa), assuming they can be lifted to their LFCs. This will be discussed further below as it relates to the effect of entrainment at different levels on parcel buoyancies. It is also interesting that the highest  $\theta_e$  profile is so close to the average  $\theta_{es}$  bin, indicating that the profiles in the highest CWV bin are close to the saturation specific humidity level of the typical atmospheric temperature profile.

### b. Buoyancy contribution for simple entraining plumes

Under the hypothesis that buoyancy effects govern the empirical relationships described above, we calculate the buoyancy per-

turbation profiles for plumes rising from the subcloud layer under various mixing assumptions. Figure 7a shows the resulting virtual temperature perturbations using original sonde data for a hypothetical parcel raised from 1000 hPa that simply conserves total water specific humidity  $q_t$  and liquid water potential temperature  $\theta_l$ , with no entrainment or loss of condensate. These individual sonde perturbation profiles have been conditionally averaged by CWV, with bin spacing as in Fig. 6.

Figure 7a shows that, without mixing, 1000 hPa parcels easily become buoyant for nearly all the bins. (The CAPE values, obtained by integrating the positive part of these curves times the gas constant over log pressure, range from near 0 to around 1,800 J kg<sup>-1</sup>). This does not correspond to the sharp increase in average precipitation shown for the three rightmost bins as seen in Fig. 3b, which have the same bin edges as in Fig. 7.

To include entrainment, we begin with a constant isobaric linear mixing with coefficient  $\chi$  of 0.1% per hPa, following Brown and Zhang (1997), and

$$r_k = (1 - \chi_{k-1})r_{k-1} + \chi_{k-1}\tilde{r}_{k-1}, \quad (1)$$

with  $r$  a conserved variable,  $\tilde{r}$  its environmental value and  $k$  denoting pressure level if  $\chi$  varies.

Brown and Zhang (1997) tuned  $\chi$  to capture cloud top height in Tropical Ocean Global Atmosphere Coupled Ocean-Atmosphere Response Experiment (TOGA COARE) data. With this mixing, the virtual temperature perturbation profiles (Fig. 7b) show a distinctive (and statistically significant) separation around the same bin in which there is a sharp increase in precipitation in Fig. 7.

To show the relative importance of subcloud versus free-tropospheric moisture on plume buoyancy, Figs. 7c,d are based on constant entrainment as above but holding  $q$  and/or temperature ( $T$ ) to constant (mean sonde) profiles in different layers. Figure 7c shows virtual temperature perturbation pro-

files for lifted parcels using a constant profile of  $q$  above 950 hPa, with  $T$  and subcloud  $q$  unchanged. Most of the bins have a reduced buoyancy above the subcloud layer, showing the importance of relatively dry air being entrained by the plume (note again that most of the bins chosen have greater than average CWV, since this is the transition region we are interested in). However, the subcloud layer moisture and  $\theta_e$ , which increase along with CWV, also have an important effect on the buoyancy, which is especially noticeable by the spread in the lower troposphere despite the identical dry air entrainment. If  $T$  is also held constant above 950 hPa (not shown), there is an even larger spread throughout the troposphere, implying that tropospheric  $T$  tends to increase with increasing CWV, most likely as a result of convection. These increasing tropospheric temperatures offset the higher parcel buoyancies due to higher  $\theta_e$  in the subcloud layer; this explains the low amount of spread in the upper troposphere seen in Fig. 7c.

The results of analysis converse to that of Fig. 7c, such that  $T$  and  $q$  are held to constant mean profiles except for  $q$  above 950 hPa, which varies as in the original sondes, are shown in Fig. 7d. Clearly, with nothing allowed to vary but the free-tropospheric moisture, there is a significant spread (as measured against standard error ranges) for mixed lifted parcels by the time they reach the upper troposphere. The parcels mixing with the driest air, from the lowest CWV bins, reach negative buoyancy rapidly in the mid-troposphere. The middle and higher bins show significant spread in the upper troposphere, and the top three bins have a small but noticeable separation from the middle ones above approximately 600 hPa. The significance of this differentiation is not certain, but the fact that these are the only three bins which remain positive above 400 hPa is intriguing.

In the lower troposphere, without the compensating effects of higher moist static energy in the subcloud layer, the bins with larger

tropospheric water actually show significantly lower buoyancy. This is because moist air is less dense than dry air of the same temperature, so, all else being equal, parcels lifted into a drier environment are more buoyant (until they entrain enough dry air to lose their high moist static energy amounts). The effect of  $q$  on virtual temperature also explains the large separation in the lower troposphere in Fig 7c. Note that the curves in Fig. 7d are much smoother than the other three panels of Fig. 7: this is because the environmental temperature, the main component of environmental virtual temperature and the main contributor to the wiggles in the difference profiles, is held constant.

A test of buoyancy profiles conditionally averaged by precipitation rather than by CWV (not shown) showed less spread and less of a trend toward higher buoyancy values with higher precipitation. This is likely due to cold pools and other processes reducing subcloud layer  $\theta_e$  during actual precipitation (indeed, the lack of trend was reduced when profiles were conditioned on precipitation occurring 3 hr after the sonde launch). Another factor is that, as Fig. 1 shows, there is less spread in tropospheric water vapor when conditionally averaged on precipitation as opposed to CWV.

## 5. Water vapor impact on buoyancy: entrainment formulation and microphysics

### *a. Sensitivity to entrainment assumptions*

The above analysis makes clear that linear mixing (used under the same assumptions, such as neglect of freezing, for which the coefficient was tuned) can yield a transition to buoyant deep convective plumes at a CWV value corresponding to the pick-up in precipitation. However, there are a number of ways in which constant mixing is unsatisfying. Jensen

and Del Genio (2006) find that a significant range of constant entrainment values are necessary to reproduce cloud top heights; Kuang and Bretherton (2006) estimate substantially larger values in CRM simulations, which if implemented in these soundings would not yield the right transition to deep convection.

Recent analysis of Large Eddy Simulations (LES) of convective boundary layers (Siebesma et al. 2007; de Roode et al. 2000; de Haij 2005) points towards a different dependence: a mixing coefficient proportional to  $z^{-1}$ , where  $z$  is height, in the layer in which plume mass flux is growing. Here we argue that such entrainment arises naturally in plume models, and leads to appealing consequences for thinking about the relative importance of different vertical layers. We then show sensitivity tests for two cases of such mixing. In section 5b we discuss the sensitivity of the buoyancy analysis to microphysics assumptions.

### 1) DEEP INFLOW MIXING

A standard continuity expression for updraft mass flux  $m$  (Stommel 1947; Siebesma et al. 2007) is

$$\frac{1}{m} \frac{\partial m}{\partial z} = \epsilon - \delta, \quad (2)$$

where  $\epsilon$  and  $\delta$  are the entrainment and detrainment rates, respectively. If a deep convective plume consists of increasing mass flux through the whole lower troposphere, with entrainment dominating detrainment, then (2) implies large lower-tropospheric entrainment rates. Such deep inflow may be seen in observed core updraft velocity to about 5 km in GATE cumulonimbus (Fig. 5 of LeMone and Zipser 1980) and in cloud-system resolving model (CRM) simulated updraft velocity up to about 6 km (Fig. 8 of Robe and Emanuel 1996). Here we seek simple examples that allow us to visualize the consequences of such “deep inflow” mixing. This can provide a contrasting approximation to “constant” mix-

ing implementations such as that used in section 4b, which effectively assume a large entrainment rate ( $m$  increases from 0 to a finite value) through the first layer, and then a much smaller rate of increase in subsequent layers.

From (2), we can compute an entrainment coefficient for any mass flux profile, if we neglect detrainment (Ogura and Cho 1973). We consider a family of mass flux profiles increasing smoothly from zero at low levels (and connecting to some other dependence in mid-troposphere):

$$m \propto z^\alpha. \quad (3)$$

An exponent  $\alpha = 1$  would be a linear increase in height, which might correspond to a lower-tropospheric response to a baroclinic wave, or to an entraining plume under circumstances outlined below. An exponent  $\alpha = 1/2$  might correspond to the  $z^{1/2}$  updraft velocities seen in dimensional arguments as early as Scorer (1957). In (2), this mass flux family yields

$$\epsilon - \delta = \alpha z^{-1}, \quad (4)$$

which corresponds to the entrainment vertical dependence of Siebesma et al. (2007).

Entrainment effects on a conserved quantity in the plume (e.g., Siebesma et al. 2007) are given by

$$\frac{\partial r}{\partial z} = \epsilon(\tilde{r} - r). \quad (5)$$

For clarity we use  $z$  coordinates here, although our computations will use the corresponding equation in pressure ( $p$ ) coordinates. Using (5) for potential temperature to diagnose entrainment rates in LES simulations of convective boundary layers (de Roode et al. 2000; de Haij 2005; Siebesma et al. 2007) led to an empirical fit for the mixing coefficient  $\epsilon = c_\epsilon z^{-1}$ , with  $c_\epsilon \approx 0.4$ – $0.55$  (Jakob and Siebesma 2003). For these boundary layer LES studies,  $\epsilon$  can contain another term that has a maximum near the trade inversion (Siebesma et al. 2007) but we omit this for the present focus on low levels of a deep convective plume.

## 2) RELATIONSHIP TO UPDRAFT VELOCITY EQUATION

For additional justification, consider an updraft velocity equation (e.g., Siebesma et al. (2007))

$$\frac{\partial w_u^2}{\partial z} = -\frac{c}{z}w_u^2 + aB, \quad (6)$$

where  $w_u$  is the updraft velocity,  $B$  is the buoyancy term, and  $c$  and  $a$  are constants. The  $z^{-1}$  in the first rhs term comes from assuming that  $\epsilon$  has the form (4). The pressure term can be considered as part of  $B$  or the coefficients depending on assumptions. Values of the coefficients will be unimportant to the results used here. A solution for this is

$$w_u^2 = z^{-c} \int_0^z a \dot{z}^c B d\dot{z}. \quad (7)$$

If  $B$  does not vary strongly with height this gives  $w_u \propto z^{1/2}$ , which yields  $c_\epsilon = \alpha = 0.5$  (neglecting detrainment, and assuming that density and plume area coverage do not change rapidly such that  $m$  has approximately the same vertical dependence of  $w_u$ ). This is close to the LES value for shallow convection (Siebesma et al. 2007; Jakob and Siebesma 2003), thus roughly explaining that value. If  $B$  instead increases linearly with height, one obtains an updraft velocity that increases roughly linearly with height,  $w_u \propto z$ . Buoyancy profiles are of course more complex, but roughly linear increases may be seen above 0.6 km in simulated CRM updrafts (Kuang and Bretherton 2006, , their Fig. 5). We note that in Fig. 7, for different CWV bins, the buoyancy through the lower troposphere can be increasing or relatively constant, and thus for sensitivity studies it is reasonable to use mixing coefficients motivated by each of these two cases.

## 3) DEEP INFLOW MIXING CASES

We thus choose two cases of mixing coefficient vertical dependence: Deep Inflow A corresponds to the Siebesma et al. (2007)

LES-based dependence; Deep Inflow B corresponds to an increase in mass flux that is linear at low levels, tapering in mid-troposphere. If detrainment is neglected, these would correspond to an exponent  $\alpha$  of 0.4 and 1, respectively, in (3) and (4). Where  $z$  and  $w$  are needed for calculations, we use the mean height and density over all sondes to convert to/from  $p$ -coordinates.

Specifically, for Deep Inflow A,

$$\chi_k = c_\epsilon z_k^{-1} \Delta z, \quad (8)$$

where  $\chi_k$  is the coefficient in (1) (which was held constant in the previous section),  $\Delta z$  is a positive finite difference layer depth, and  $c_\epsilon = 0.4$ .

For Deep Inflow B, we choose a lower-tropospheric  $w_u$  profile that increases nearly linearly at low levels, namely a quarter sine wave in  $z$  with zero at 1000 hPa and maximum at 430 hPa (7 km). This roughly approximates the Robe and Emanuel (1996) updraft velocities, and is loosely consistent with observational studies of convective regions (e.g., LeMone and Zipser 1980; Cifelli and Rutledge 1994; LeMone and Moncrieff 1994). Small variations of the  $m$ -profile shape have little overall effect, and the magnitude is irrelevant. Mixing coefficients are computed from the  $p$ -coordinate version of (2), neglecting entrainment, using  $\chi_k = -m^{-1}(\partial m / \partial p) \Delta p$ , with  $\Delta p$  defined positive. Below 900 hPa, where small mass flux requires caution in finite differencing, we use analytical results from (10) below, yielding  $\chi_k = (p_0 - p_k)^{-1} \Delta p$ . Above 430 hPa, where the mass flux no longer increases, entrainment is set to zero for simplicity.

## 4) VERTICAL WEIGHTING OF ENVIRONMENTAL VALUES

For a plume increasing from zero mass flux at pressure  $p_0$  the value of conserved quantity  $r$  within the plume at level  $p$  is related

to the environmental value  $\tilde{r}$  by

$$r(p) = \frac{1}{m(p)} \int_{p_0}^p \tilde{r} \frac{\partial m}{\partial p} d\hat{p}, \quad (9)$$

from the  $p$ -coordinate version of (5) and neglecting detrainment in (2). The vertical rate of increase of mass gives the weighting of the environmental variable. For the case of a linearly increasing plume  $m = c(p_0 - p)$ , this reduces to the vertical average over all levels below:

$$r(p) = (p - p_0)^{-1} \int_{p_0}^p \tilde{r} d\hat{p}. \quad (10)$$

Therefore, although  $\epsilon$  and  $\chi$  decrease rapidly above the surface, this linear case shows that this does not necessarily result in strong dependence on near-surface values. Equal increments of mass are brought into the plume at each level, and the apparent high entrainment is simply because the mass flux is small near the surface. This can also be thought of as plumes rising more slowly having more time for dilution, related to the Neggers et al. (2002) argument for modeling entrainment rates as the inverse of updraft velocity.

This linear case further makes clear why CWV is a very reasonable indicator of buoyancy for deep entraining plumes. For this mass-flux profile, mid-tropospheric buoyancy depends on the environmental water vapor vertically integrated through the lower troposphere, a quantity similar to CWV. Different mass flux profiles yield different vertical weighting. For instance, for  $z^\alpha$ , the weighting is  $z^{\alpha-1}$ , which weights lower levels more heavily (when  $\alpha < 1$ ). For  $\alpha = 1/2$ , and linear decrease in the environmental variable, the level equivalent to the weighted mean occurs at  $(p - p_0)/3$ , instead of  $(p - p_0)/2$ . However, even when the vertical mean is not the optimal weighting, CWV will be a reasonable buoyancy estimator for any mass flux increasing through a deep lower-tropospheric layer, especially given the preponderance of variance

occurring in the lower free troposphere.

## 5) SENSITIVITY TO DEEP INFLOW MIXING PROFILES

Figures 8a,b show entraining plume buoyancy profiles resulting from Deep Inflow A and Deep Inflow B cases. Although these different mixing profiles show different values in Fig. 8 for the exact level of sign change (neutral buoyancy) for the different buoyancy profiles, the qualitative spread and order of the curves is not much different among these two mixing schemes or from those in the buoyancy profiles for the constant mixing in Fig. 7b. As in the constant mixing case, only the top few curves (corresponding to the precipitation pick-up in Fig. 3b) are buoyant at certain levels (although the vertical levels for which this is true are lower in these latter two mixing cases—the inclusion of ice processes discussed in section 5b below offers one explanation for this). There is less sensitivity to 1000 hPa  $\theta_e$  in these vertically dependent mixing cases, as should be expected given the greater emphasis placed on entraining lower-tropospheric air through a relatively deep layer.

For Deep Inflow B (Fig. 8b), few CWV bins have buoyant shallow cumulus plumes, but this is not surprising since strong entrainment occurs through the whole lower troposphere. For shallow cumulus, the Deep Inflow A profile—or the full LES-based mixing profile of Siebesma et al. (2007)—is likely more suitable.

Even more than the Deep Inflow A mixing scheme, the Deep Inflow B scheme places importance on all of the lower-tropospheric values, not just the subcloud layer. Since CWV captures variance throughout the lower free troposphere, but includes contributions from the subcloud layer as well, CWV would be a good predictor of buoyancy if real mixing occurred as described by the deep inflow theory, for locations that already have wind profiles typical of deep convection regions. As men-

tioned above, (10) results in equal weighting of all lower-tropospheric levels in the plume buoyancy, implying that CWV, which weights many lower-tropospheric environmental moisture levels, should indeed be a good indicator of deep convection and precipitation.

*b. Sensitivity to microphysics assumptions*

An analysis of the sensitivity of the above buoyancy profiles to microphysics assumptions reveals a large amount of uncertainty in the specific values of buoyancy, though not in the monotonic order of the curves. Figures 8c,d show the effects of including ice mixing above the freezing level for the Deep Inflow A and Deep Inflow B mixing schemes, respectively. The mixing process is similar to that used above, except that instead of conserving the liquid water potential temperature,  $\theta_l$ , we instead conserve the ice-liquid water potential temperature,  $\theta_{il}$  (Bryan and Fritsch 2004, their Eq. 23). This reduces to the reversible liquid water potential temperature used above (from Emanuel 1994) when there is no ice. To make the contribution from freezing obvious, all liquid is converted to ice when the plume reaches 0°C; this is the only irreversible process other than the mixing, and is accomplished by equating the total enthalpies of all states before and after the freezing process (Emanuel 1994). The rapid freezing is chosen to make the warming associated with freezing clear in the plots. Implementing the phase change gradually between 0 and -40°C (e.g., Raymond and Blyth 1992; Bryan and Fritsch 2004) would spread this warming through a layer extending upward to about 250 hPa.

The curves including ice for the top CWV bins in Figs. 8c,d are buoyant throughout the troposphere; in the Deep Inflow B case, only the top two CWV curves retain their buoyancy, though the third-highest bin becomes only slightly negatively buoyant through a portion of the lower troposphere. Buoyancy above the freezing level for plumes that are

negatively buoyant below is unlikely to be realized in practice. Again, the Deep Inflow B mixing is not appropriate for shallow convection, as seen by the lack of shallow buoyant plumes in Fig. 8d. In both of these ice cases, there is still a large separation in the curves corresponding to CWV, and a particularly noticeable separation between the top three bins and the lower ones, as discussed in previous figures. This again relates well to the precipitation pick-up seen in Fig. 3. The constant mixing case, with freezing included, would not correspond well to this pick-up, since most bins would yield deep convection.

Another aspect of microphysics that affects the buoyancy values of mixing profiles is the treatment of hydrometeors. In all of the above analyses, all liquid and/or ice is retained in the mixed parcels (though of course  $q_t$  is one of the mixed variables). Using a pseudo-adiabatic entropy as the conserved variable above saturation, and thereby removing condensate and its effects on buoyancy, tends to increase the buoyancy by as much as 2 K in the mid-troposphere, with lower increases above and below this, and with slight decreases at very high levels (figure not shown). This level of sensitivity to hydrometeor removal, as well as the sensitivity seen for ice processes above, is broadly consistent with the approximately 3 K differences seen in Raymond and Blyth (1992). Again, the order and separation of the curves is not affected much. The positive change comes from the removal of condensate loading in the virtual temperature calculation, while the reduction and eventual reversal of that change at upper levels reflects the lack of additional enthalpy transferred from condensate to air (Emanuel 1994). While the removal of all condensate below the freezing level is unrealistic, above that level it is expected that some of the additional buoyancy gained from the removal of condensate could further increase the strength of updrafts.

*c. Sensitivity to column temperature and relative humidity*

The relationship between moisture and precipitation should depend on temperature. For this deep tropical location, temperature variations are small enough that they could be ignored to a first approximation. This was addressed in Fig. 2a and Fig. 4b, showing that most of the changes of  $q$  associated with changes in CWV are due to changes in relative humidity, not to changes in temperature.

A plausible next approximation might be to consider column relative humidity (the ratio of CWV to saturation CWV) following Bretherton et al. (2004). However, the rapid pick-up in precipitation actually has a different temperature dependence (Neelin et al. 2008), occurring at a subsaturation that increases with temperature.

We examined both possibilities in the ARM sonde data. The analyses of Fig. 3, Fig. 7 and Fig. 8 were repeated (i) using column relative humidity; (ii) binning the data by 1000–200 hPa column average temperature (with 1 K width). The precipitation pick-up occurred with similar magnitude to Fig. 3 for all cases, and the shifts as a function of temperature appeared consistent with those in (Neelin et al. 2008), whereas normalization by saturation CWV caused overcompensation. However, the results of these analyses were noisy because of small sample size, even for bins only 1 K from the mean. Definitive results would require data through a larger range of temperatures. The buoyancy relationships were noisy as well, but the spread was similar to Fig. 7.

## 6. Conclusions

Five years of radiosonde and precipitation gauge data from Nauru Island are used to examine the relationship of the vertical structure of water vapor to tropical deep convection. The leading vertical principal component of specific humidity, which is highly cor-

related with CWV, peaks in the lower troposphere around 800 hPa and has a relatively small contribution from subcloud levels. The variances associated with CWV are due predominantly to fluctuations in relative humidity, not to changes in temperature at constant relative humidity. Although there is a larger average amount of partial CWV contained between the surface and 850 hPa than there is above 850 hPa, nearly all CWV variance can be explained by the variance in the layer above 850 hPa. The boundary layer contains slightly more water vapor but, since it is tied closely to the surface by turbulent and convective processes, its variance is much smaller, and that smaller variance is itself correlated with the free-tropospheric variance.

Moisture profiles conditionally averaged on precipitation show a strong association between rainfall and moisture variability in the free troposphere, and little boundary layer variability. When precipitation is conditionally averaged on CWV, a sharp pick-up occurs at high enough CWV, consistent with other observational studies (Bretherton et al. 2004; Peters and Neelin 2006). Furthermore, this same pick-up can be reproduced by conditionally averaging precipitation only on the partial CWV from 850–200 hPa, while averaging only on subcloud layer (below 950 hPa) water vapor shows little corresponding response in precipitation. This suggests that moisture above the boundary layer is the key component in the relationship between CWV and the transition to deep convection and higher average precipitation rates.

Because CWV is widely observed from satellite retrievals, we seek to understand why it proves such a useful indicator of favorable conditions for tropical deep convection. The buoyancy of plumes rising under different conditions, for several entrainment assumptions, provides insight. The transition to high precipitation rates at sufficiently high CWV appears to depend primarily on free-tropospheric moisture, which can greatly af-

fect the buoyancy of lifted parcels undergoing entrainment. There is also a dependence on the small but significant correlation between CWV and subcloud layer moisture and  $\theta_e$ .

Entraining plumes tend to be far more buoyant at middle and upper levels for profiles with larger CWV values. This is robust for all three mixing profiles analyzed, although the level at which positively buoyant parcels reach neutral buoyancy differs, as does the relative weighting of entrainment from the free troposphere and boundary layer. Constant mixing, similar to many convective parameterizations, must be rather small to not kill convection by the time it reaches the middle troposphere, and thus tends to emphasize boundary layer  $\theta_e$ . Using mixing values from Brown and Zhang (1997) can give the transition to deep convection at the approximate CWV value at which precipitation picks up, but only if freezing is neglected. Two “deep-inflow” mixing profiles based on increasing mass flux through a deep lower-tropospheric layer are considered. One is based on LES studies of entrainment in convective boundary layers (Siebesma et al. 2007), and a second assumes entrainment associated with a mass flux profile increasing linearly at low levels, to a maximum at mid-troposphere. Both yield the increase in buoyancy as a function of CWV. When simple freezing physics is included, the deep inflow mixing cases both give better correspondence than constant mixing between the pick-up in precipitation in the upper few CWV bins and buoyancy available for deep convection. Analytic results for these mixing profiles show how buoyancy in the mid-troposphere depends on a weighted vertical average over the lower troposphere; in the case of a linearly growing plume, all lower-tropospheric levels are weighted equally. In the presence of such entrainment, CWV is thus a very reasonable measure of the buoyancy available to a deep convective plume.

These results underline the key role that free-tropospheric moisture plays in the tran-

sition from shallow to deep convection. The observed pick-up of precipitation with CWV is linked to increased buoyancy of entraining plumes, and the importance of accurately representing the entrainment process to obtain this sensitivity is shown. This adds an observational constraint on entrainment that may be useful in revising GCM convective parameterizations, and points toward entrainment schemes associated with more realistic mass flux profiles than the commonly used constant mixing.

#### *Acknowledgments.*

This work was supported in part by National Science Foundation ATM-0082529, National Oceanic and Atmospheric Administration NA05OAR4311134. JDN acknowledges the John Simon Guggenheim Memorial Foundation and the National Center for Atmospheric Research for sabbatical support. CEH was supported by NASA Earth System Science Fellowship Grant NNX06AF83H. We thank K. Emanuel, M. Hughes, B. Lesht, B. Medeiros, R. Neale, L. Nuijens, B. Stevens, J. Tribbia, X. Wu, and G. Zhang for discussions and J. Meyerson for graphical assistance.

## References

- Biasutti, M., A. H. Sobel, and Y. Kushnir, 2006: AGCM precipitation biases in the tropical Atlantic. *J. Climate*, **19**, 935–958.
- Bretherton, C. S., M. E. Peters, and L. E. Back, 2004: Relationships between water vapor path and precipitation over the tropical oceans. *J. Climate*, **17**, 1517–1528.
- Brown, R. G. and C. Zhang, 1997: Variability of midtropospheric moisture and its effect on cloud-top height distribution during TOGA COARE. *J. Atmos. Sci.*, **54**, 2760–2774.
- Bryan, G. H. and J. M. Fritsch, 2004: A reevaluation of ice-liquid water potential temperature. *Mon. Wea. Rev.*, **132**, 2421–2431.
- Cifelli, R. and S. Rutledge, 1994: Vertical motion structure in maritime continent mesoscale convective systems: results from a 50-MHz profiler. *J. Atmos. Sci.*, **51**, 2631–2652.
- Dai, A., 2006: Precipitation characteristics in eighteen coupled climate models. *J. Climate*, **19**, 4605–4630.
- de Haij, M. J., 2005: Evaluation of a new trigger function for cumulus convection. Tech. Rep. TR-276, KNMI, De Bilt, Netherlands, 117 pp.
- de Roode, S. R., P. G. Duynkerke, and A. P. Siebesma, 2000: Analogies between mass-flux and reynolds-averaged equations. *J. Atmos. Sci.*, **57**, 1585–1598.
- DeMott, C. A. and S. Rutledge, 1998: The vertical structure of TOGA COARE convection. Part II: Modulating influences and implications for diabatic heating. *J. Atmos. Sci.*, **55**, 2748–2762.
- Derbyshire, S. H., I. Beau, P. Bechtold, J.-Y. Grandpeix, J.-M. Piriou, J.-L. Redelsperger, and P. M. M. Soares, 2004: Sensitivity of moist convection to environmental humidity. *Quart. J. Roy. Meteor. Soc.*, **130**, 3055–3080.
- Emanuel, K. A., 1994: *Atmospheric Convection*. 1st ed., Oxford University Press, New York, 580 pp.
- Grabowski, W. W., 2003: MJO-like coherent structures: Sensitivity simulations using the Cloud-Resolving Convection Parameterization (CRCP). *J. Atmos. Sci.*, **60**, 847–864.
- , 2006: Impact of explicit atmosphere-ocean coupling on MJO-like coherent structures in idealized aquaplanet simulations. *J. Atmos. Sci.*, **63**, 2289–2306.
- Holloway, C. E. and J. D. Neelin, 2007: The convective cold top and quasi equilibrium. *J. Atmos. Sci.*, **64**, 1467–1487.
- Jakob, C. and A. P. Siebesma, 2003: A new subcloud model for mass-flux convection schemes: influence on triggering, updraft properties, and model climate. *Mon. Wea. Rev.*, **131**, 2765–2778.
- Jensen, M. P. and A. D. Del Genio, 2006: Factors limiting convective cloud-top height at the ARM Nauru Island Climate Research Facility. *J. Climate*, **19**, 2105–2117.
- Kuang, Z. and C. S. Bretherton, 2006: A mass-flux scheme view of a high-resolution simulation of a transition from shallow to deep cumulus convection. *J. Atmos. Sci.*, **63**, 1895–1909.
- LeMone, M. A. and M. W. Moncrieff, 1994: Momentum and mass transport by convective bands: Comparisons of highly idealized dynamical models to observations. *J. Atmos. Sci.*, **51**, 281–305.
- LeMone, M. A. and E. J. Zipser, 1980: Cumulonimbus vertical velocity events in GATE.

- Part I: Diameter, intensity and mass flux. *J. Atmos. Sci.*, **37**, 2444–2457.
- Lintner, B. R. and J. D. Neelin, 2007: A prototype for convective margin shifts. *Geophys. Res. Lett.*, **34** (L05812), 5, doi: 10.1029/2006GL027305.
- Liu, W. T., W. Tang, and P. P. Niiler, 1991: Humidity profiles over the ocean. *J. Climate*, **4**, 1023–1034.
- Mapes, B. E. and P. Zuidema, 1996: Radiative-dynamical consequences of dry tongues in the tropical troposphere. *J. Atmos. Sci.*, **53**, 620–638.
- Mather, J. H., T. P. Ackerman, W. E. Clements, F. J. Barnes, M. D. Ivey, L. D. Hatfield, and R. M. Reynolds, 1998: An atmospheric radiation and cloud station in the tropical western Pacific. *Bull. Amer. Meteor. Soc.*, **79**, 627–642.
- Neelin, J. D., 1997: *The physics and parameterization of moist atmospheric convection*, chap. Implications of convective quasi-equilibrium for the large-scale flow, 413–416. Kluwer Academic Publishers, Dordrecht, The Netherlands.
- Neelin, J. D., C. Chou, and H. Su, 2003: Tropical drought regions in global warming and El Niño teleconnections. *Geophys. Res. Lett.*, **30** (24), 2275, doi: 10.1029/2003GL018625.
- Neelin, J. D., M. Munnich, H. Su, J. E. Meyer-son, and C. E. Holloway, 2006: Tropical drying trends in global warming models and observations. *Proc. Nat. Acad. Sci.*, **103**, 6110–6115.
- Neelin, J. D., O. Peters, J. W.-B. Lin, K. Hales, and C. E. Holloway, Accepted 2008: Rethinking convective quasi-equilibrium: Observational constraints for stochastic convective schemes in climate models. *Phil. Trans. Roy. Soc. Lond. A*.
- Neelin, J. D. and N. Zeng, 2000: A quasi-equilibrium tropical circulation model—formulation. *J. Atmos. Sci.*, **57**, 1741–1766.
- Neggers, R., J. D. Neelin, and B. Stevens, 2007: Impact mechanisms of shallow cumulus convection on tropical climate dynamics. *J. Climate*, **20**, 2623–2642.
- Neggers, R. A. J., A. P. Siebesma, and H. J. J. Jonker, 2002: A multiparcel model for shallow cumulus convection. *J. Atmos. Sci.*, **59**, 1655–1668.
- Numaguti, A., R. Oki, K. Nakamura, K. Tsuboki, N. Misawa, T. Asai, and Y.-M. Kodama, 1995: 4-5-day-period variation on low-level dry air observed in the equatorial western Pacific during the TOGA COARE IOP. *J. Meteor. Soc. Japan*, **73**, 267–290.
- Ogura, Y. and H. R. Cho, 1973: Diagnostic determination of cumulus cloud populations from observed large-scale variables. *J. Atmos. Sci.*, **30**, 1276–1286.
- Parsons, D. B., K. Yoneyama, and J.-L. Redelsperger, 2000: The evolution of the tropical western Pacific atmosphere-ocean system following the arrival of a dry intrusion. *Quart. J. Roy. Meteor. Soc.*, **126**, 517–548.
- Peters, O. and J. D. Neelin, 2006: Critical phenomena in atmospheric precipitation. *Nature Physics*, **2**, 393–396.
- Raymond, D. J., 1997: Boundary layer quasi-equilibrium (BLQ). *The Physics and Parameterization of Moist Atmospheric Convection*, Smith, R. K., Ed., Kluwer Academic Publishers, 387–397.
- , 2000: Thermodynamic control of tropical rainfall. *Quart. J. Roy. Meteor. Soc.*, **126**, 889–898.
- Raymond, D. J. and A. M. Blyth, 1992: Extension of the stochastic mixing model to cumulonimbus clouds. *J. Atmos. Sci.*, **49**, 1968–1983.

- Robe, F. R. and K. A. Emanuel, 1996: Moist convective scaling: Some inferences from three-dimensional cloud ensemble simulations. *J. Atmos. Sci.*, **53**, 3265–3275.
- Scorer, R. S., 1957: Experiments on convection of isolated masses of buoyant fluid. *J. Fluid Mech.*, **2**, 583–594.
- Siebesma, A. P., P. M. M. Soares, and J. Teixeira, 2007: A combined eddy diffusivity mass flux approach for the convective boundary layer. *J. Atmos. Sci.*, **64**, 1230–1248.
- Slingo, J. M., K. R. Sperber, J. S. Boyle, J.-P. Ceron, and coauthors, 1996: Intraseasonal oscillation in 15 atmospheric general circulation models: Results from an AMIP diagnostic subproject. *Climate Dynamics*, **12**, 325–357.
- Sobel, A. H. and J. D. Neelin, 2006: The boundary layer contribution to intertropical convergence zones in the quasi-equilibrium tropical circulation model framework. *Theoretical and Computational Fluid Dynamics*, **20**, 323–350.
- Sobel, A. H., S. E. Yuter, C. S. Bretherton, and G. N. Kiladis, 2004: Large-scale meteorology and deep convection during TRMM KWAJEX. *Mon. Wea. Rev.*, **132**, 422–444.
- Stokes, G. M. and S. E. Schwartz, 1994: The Atmospheric Radiation Measurement (ARM) Program: Programmatic background and design of the cloud and radiation testbed. *Bull. Amer. Meteor. Soc.*, **75**, 1201–1221.
- Stommel, H., 1947: Entrainment of air into a cumulus cloud. *J. Meteor.*, **4**, 91–94.
- Tompkins, A. M., 2001a: Organization of tropical convection in low vertical wind shears: The role of cold pools. *J. Atmos. Sci.*, **58**, 1650–1672.
- , 2001b: Organization of tropical convection in low vertical wind shears: The role of water vapor. *J. Atmos. Sci.*, **58**, 529–545.
- Westwater, E. R., B. B. Stankov, D. Cimini, Y. Han, J. A. Shaw, B. M. Lesht, and C. N. Long, 2003: Radiosonde humidity soundings and microwave radiometers during Nauru99. *J. Atmos. Oceanic Technol.*, **20**, 953–971.
- Xu, K.-M. and K. A. Emanuel, 1989: Is the tropical atmosphere conditionally unstable? *Mon. Wea. Rev.*, **117**, 1471–1479.
- Yoneyama, K., 2003: Moisture variability over the tropical western Pacific ocean. *J. Meteor. Soc. Japan*, **81**, 317–337.
- Zhang, G. J. and H. Wang, 2006: Toward mitigating the double ITCZ problem in NCAR CCSM3. *Geophys. Res. Lett.*, **33**, L06709, doi:10.1029/2005GL025229.

# List of Figures

- 1 Specific humidity ( $\text{g kg}^{-1}$ ) profiles conditionally averaged on 1-hr average precipitation rate in  $\text{mm hr}^{-1}$  (color bar). Bin counts from lowest to highest precipitation range are: 2805, 93, 90, 59, 32, 40, 36, 49, 47, 43, 44, 30, 21, and 11. Horizontal bars indicate the maximum, as well as a representative,  $\pm 1$  standard error (standard deviation divided by the square root of the sample number) range. 21
- 2 (a) Variance of specific humidity ( $\text{g}^2 \text{kg}^{-2}$ ) for all sondes (red) and for sondes within  $\pm 3$  hours of the highest precipitation averages (blue). Long-dashed lines show total variance, solid lines show variance explained by PC 1 at each level. The dotted red line shows total variance at each level of a hypothetical specific humidity field derived only from temperature and a fixed relative humidity profile (taken from the mean of all original sonde relative humidity). (b) Fractional variance explained by PC 1. (c) Scatter plots and linear regressions of the integrated contribution to column water (mm) from the surface to 850 hPa (magenta) and from 850–200 hPa (green) versus the column water vapor. (d) Regressions and correlations of PC 1 versus column water vapor for all sondes (top) and for sondes within  $\pm 3$  hours of the highest 1-hr precipitation (bottom). 22
- 3 Specific humidity ( $\text{g kg}^{-1}$ ) profiles and 1-hr average precipitation rates, respectively, conditionally averaged on: (a), (b) total column water vapor in mm (color bar); (c), (d) column water integrated from 850–200 hPa (color bar); and (e), (f) column water integrated from the surface to 950 hPa (color bar). Vertical bars on precipitation values represent  $\pm 1$  standard error. Horizontal bars indicate limits of the maximum, as well as a representative, standard error range. Inset for panel (a) shows number of sondes for total column water vapor bins plotted against each bin’s average value. . . . . 23
- 4 Relative humidity (%) profiles conditionally averaged on: (a) 1-hr average precipitation rate in  $\text{mm hr}^{-1}$  (color bar); (b) column water vapor in mm (color bar). Horizontal bars indicate limits of the maximum, as well as a representative, standard error range below 150 hPa. . . . . 24
- 5 Humidity anomalies (taken as differences from the highly populated bin with precipitation less than  $0.0025 \text{ mm hr}^{-1}$ ) for precipitation above  $2.56 \text{ mm hr}^{-1}$  lagging (before rain) and leading (after rain) the radiosonde by up to three hours, for: (a), (b) specific humidity ( $\text{g kg}^{-1}$ ) profiles; (c), (d) relative humidity (%) profiles. Horizontal bars on right show maximum standard error range for panels (a) and (b), while for panels (c) and (d) they represent the characteristic standard error range for three main vertical regions, with maximums shown in the upper troposphere. . . . . 25
- 6 Profiles of reversible (a)  $\theta_e$  (K) and (b)  $\theta_{es}$  (K). These are conditioned on column water vapor in mm (color bar). The dashed black line, reproduced in each panel, is the bin-count-weighted mean  $\theta_{es}$  profile for all bins greater than 50 mm. Horizontal bars indicate limits of the maximum, as well as a representative, standard error range below 150 hPa. . . . . 26

- 7 Virtual temperature (K) difference profiles conditionally averaged on initial sonde column water vapor in mm (color bar), where the environmental (initial) sonde virtual temperature is subtracted from a profile determined by lifting a 1000-hPa parcel conserving total water and liquid equivalent potential temperature but also including: (a) no environmental mixing; (b) constant 0.5% mixing; (c) mixing with adjusted sonde profiles using mean specific humidity for levels above 950 hPa; (d) mixing with an adjusted sonde profile using mean temperature for all levels and mean specific humidity for levels below 950 hPa. Horizontal bars indicate limits of the maximum, as well as a representative, standard error range below 150 hPa (note that these bars appear on the side in panel (d) for visual clarity). For a few sondes in (c) and (d),  $q$  values have been slightly reduced at a few levels to remove supersaturation. . . . . 27
- 8 Virtual temperature (K) difference profiles conditionally averaged on initial sonde column water vapor in mm (color bar), where the environmental (initial) sonde virtual temperature is subtracted from a profile determined by lifting a 1000-hPa parcel conserving total water and liquid equivalent potential temperature but also including: (a) Deep Inflow A mixing; (b) Deep Inflow B mixing; (c) Deep Inflow A mixing with conversion of liquid to ice, and following an ice-vapor reversible adiabat, above the freezing layer; (d) same as (c), but for Deep Inflow B mixing. In (c) and (d), the jumps in virtual temperature difference at the freezing level for all but the 1 uppermost and 2 lowermost column water vapor bins have been extended from about 10–15 hPa to 30 hPa, with a straight line connecting the otherwise original upper and lower curves, for visual clarity. Horizontal bars indicate limits of the maximum, as well as a representative, standard error range below 150 hPa. . . . . 28

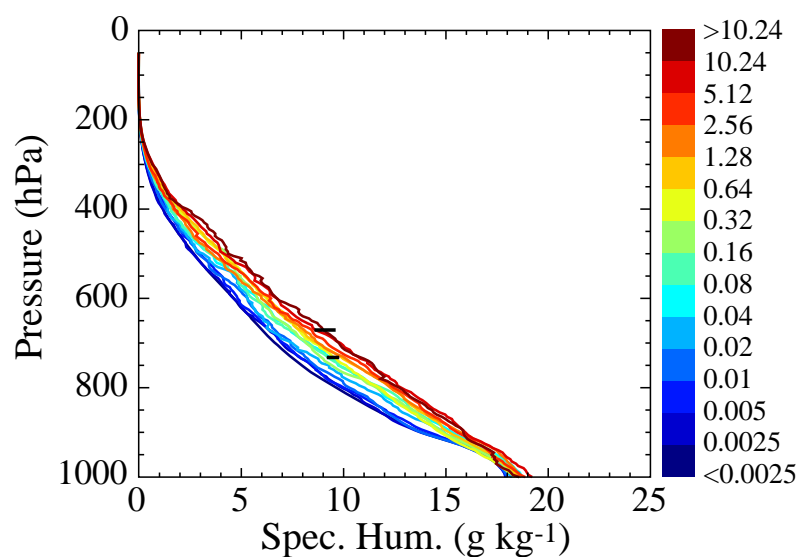


FIG. 1. Specific humidity ( $\text{g kg}^{-1}$ ) profiles conditionally averaged on 1-hr average precipitation rate in  $\text{mm hr}^{-1}$  (color bar). Bin counts from lowest to highest precipitation range are: 2805, 93, 90, 59, 32, 40, 36, 49, 47, 43, 44, 30, 21, and 11. Horizontal bars indicate the maximum, as well as a representative,  $\pm 1$  standard error (standard deviation divided by the square root of the sample number) range.

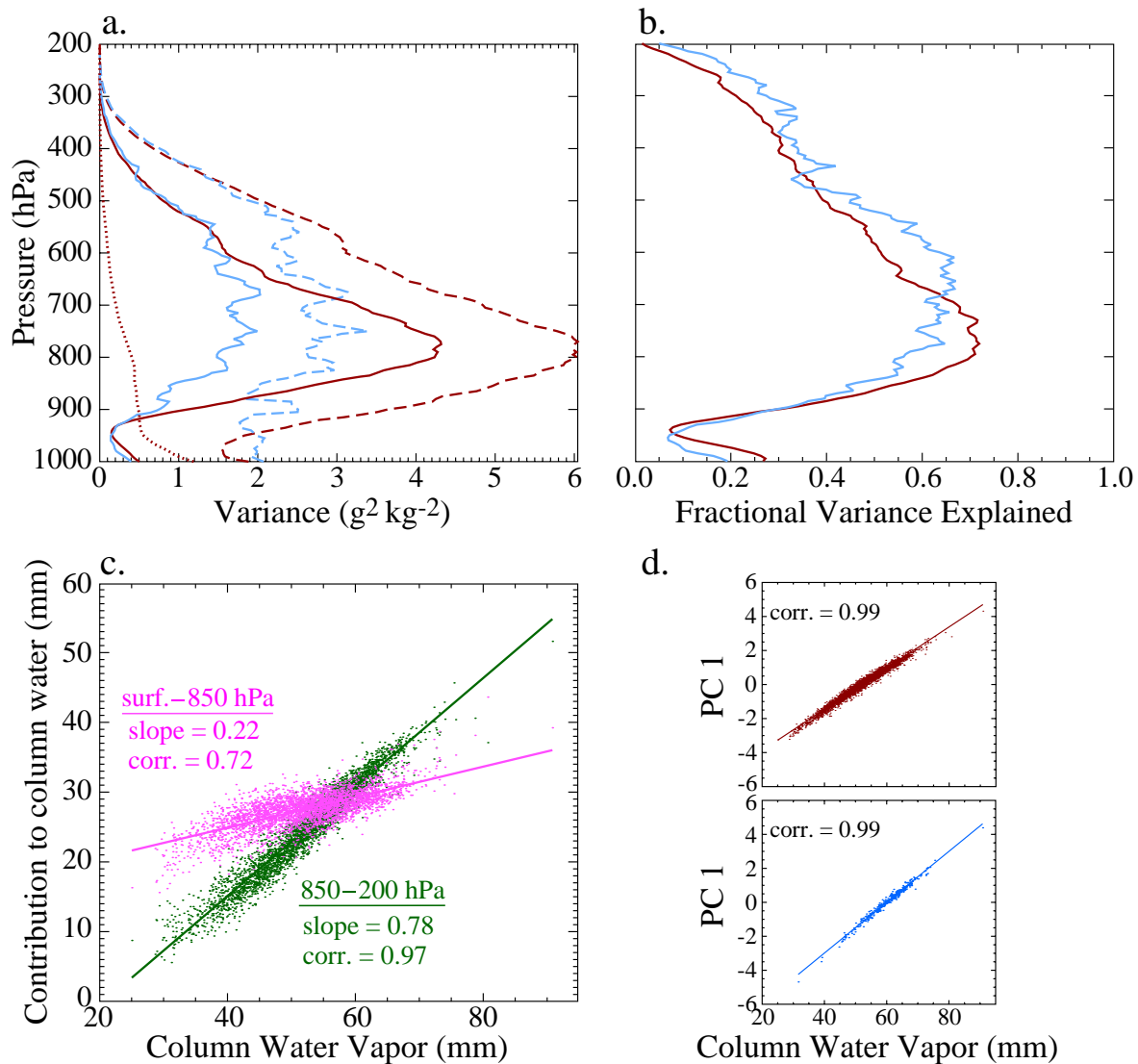


FIG. 2. (a) Variance of specific humidity ( $\text{g}^2 \text{kg}^{-2}$ ) for all sondes (red) and for sondes within  $\pm 3$  hours of the highest precipitation averages (blue). Long-dashed lines show total variance, solid lines show variance explained by PC 1 at each level. The dotted red line shows total variance at each level of a hypothetical specific humidity field derived only from temperature and a fixed relative humidity profile (taken from the mean of all original sonde relative humidity). (b) Fractional variance explained by PC 1. (c) Scatter plots and linear regressions of the integrated contribution to column water (mm) from the surface to 850 hPa (magenta) and from 850–200 hPa (green) versus the column water vapor. (d) Regressions and correlations of PC 1 versus column water vapor for all sondes (top) and for sondes within  $\pm 3$  hours of the highest 1-hr precipitation (bottom).

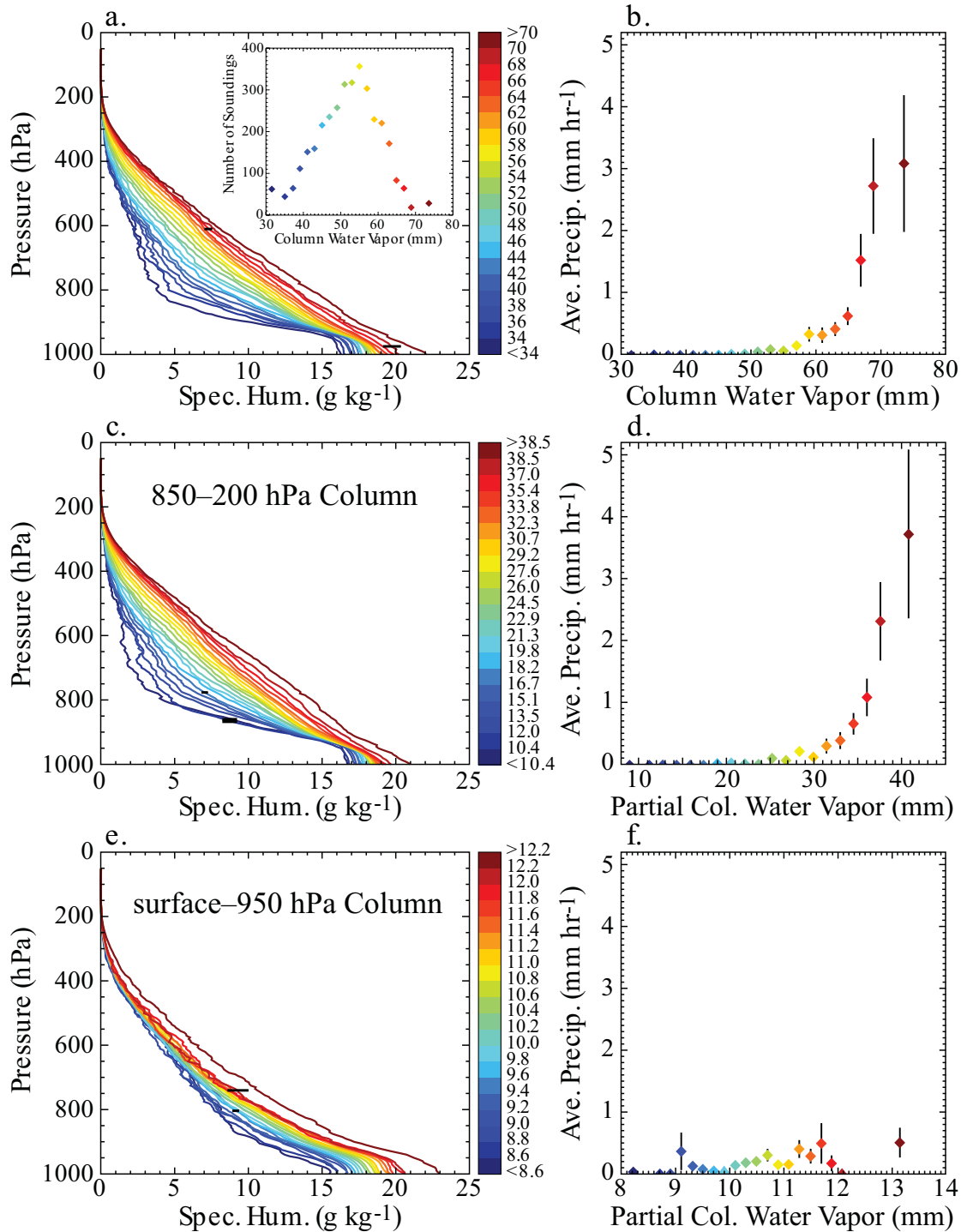


FIG. 3. Specific humidity ( $\text{g kg}^{-1}$ ) profiles and 1-hr average precipitation rates, respectively, conditionally averaged on: (a), (b) total column water vapor in mm (color bar); (c), (d) column water integrated from 850–200 hPa (color bar); and (e), (f) column water integrated from the surface to 950 hPa (color bar). Vertical bars on precipitation values represent  $\pm 1$  standard error. Horizontal bars indicate limits of the maximum, as well as a representative, standard error range. Inset for panel (a) shows number of sondes for total column water vapor bins plotted against each bin's average value.

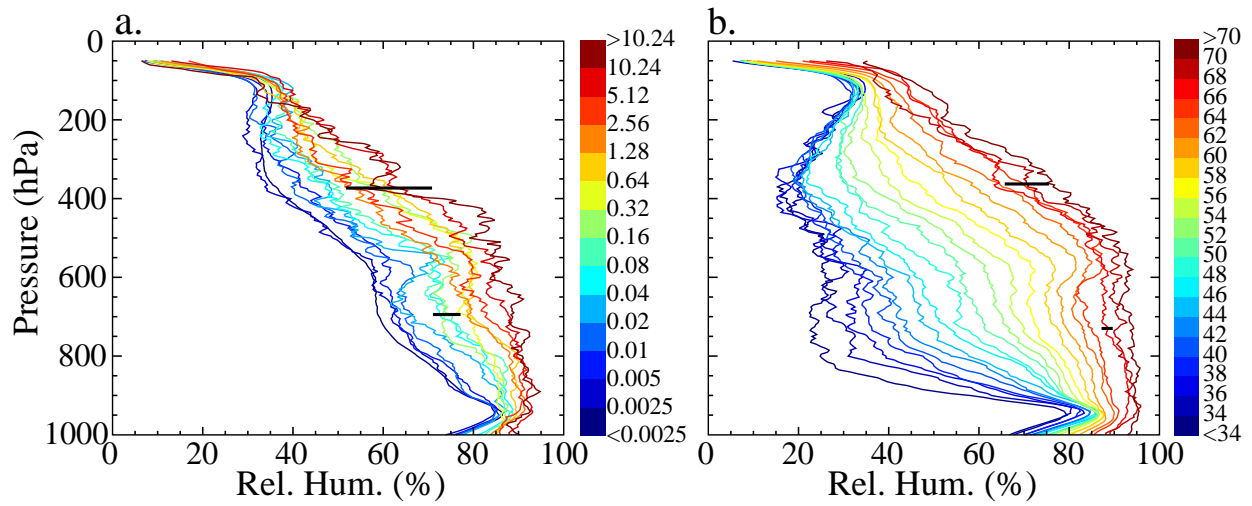


FIG. 4. Relative humidity (%) profiles conditionally averaged on: (a) 1-hr average precipitation rate in  $\text{mm hr}^{-1}$  (color bar); (b) column water vapor in mm (color bar). Horizontal bars indicate limits of the maximum, as well as a representative, standard error range below 150 hPa.

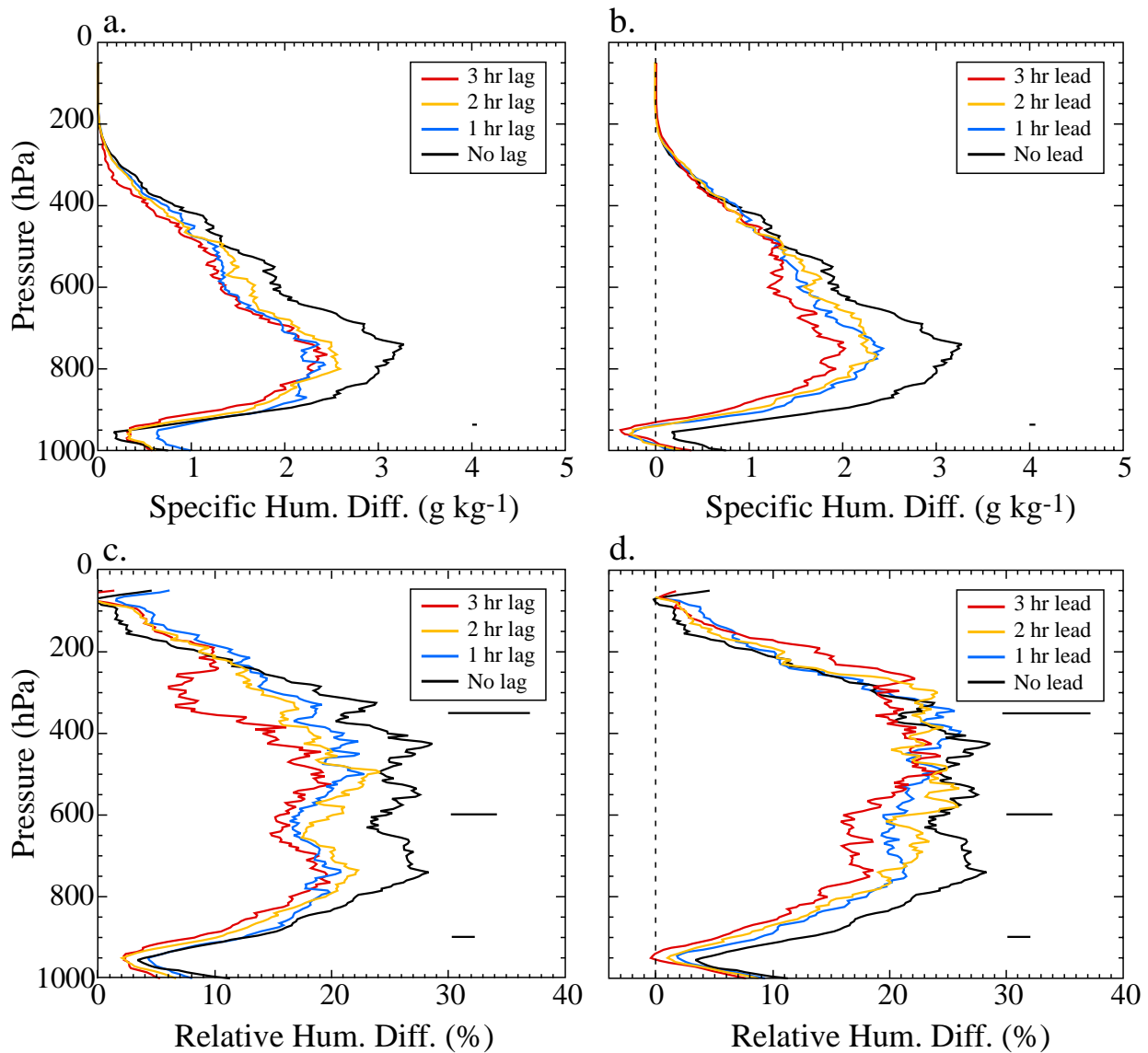


FIG. 5. Humidity anomalies (taken as differences from the highly populated bin with precipitation less than  $0.0025 \text{ mm hr}^{-1}$ ) for precipitation above  $2.56 \text{ mm hr}^{-1}$  lagging (before rain) and leading (after rain) the radiosonde by up to three hours, for: (a), (b) specific humidity ( $\text{g kg}^{-1}$ ) profiles; (c), (d) relative humidity (%) profiles. Horizontal bars on right show maximum standard error range for panels (a) and (b), while for panels (c) and (d) they represent the characteristic standard error range for three main vertical regions, with maximums shown in the upper troposphere.

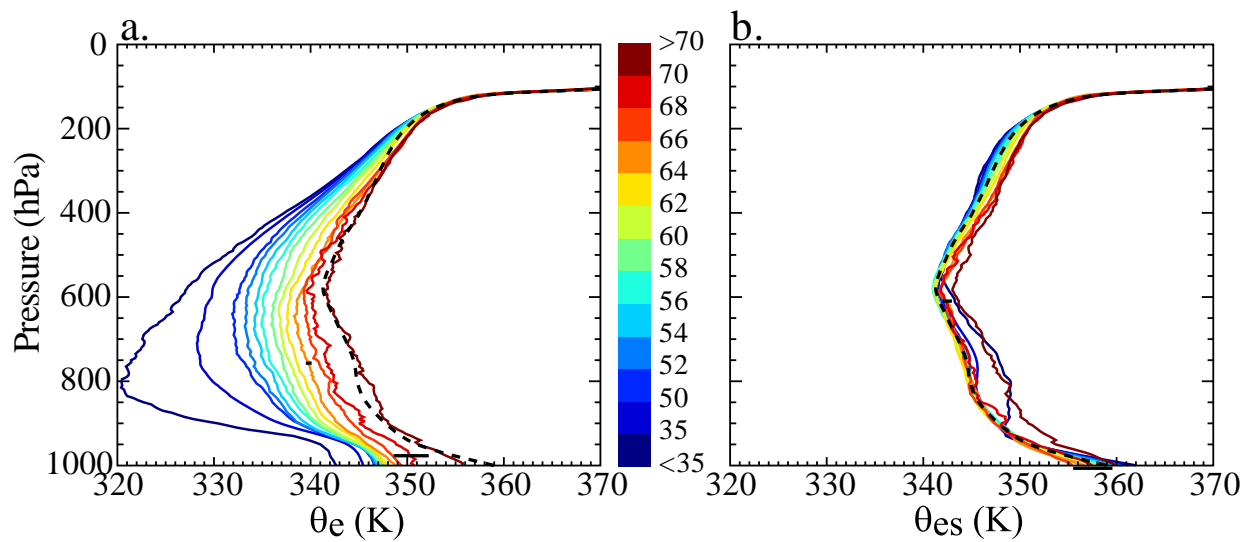


FIG. 6. Profiles of reversible (a)  $\theta_e$  (K) and (b)  $\theta_{es}$  (K). These are conditioned on column water vapor in mm (color bar). The dashed black line, reproduced in each panel, is the bin-count-weighted mean  $\theta_{es}$  profile for all bins greater than 50 mm. Horizontal bars indicate limits of the maximum, as well as a representative, standard error range below 150 hPa.

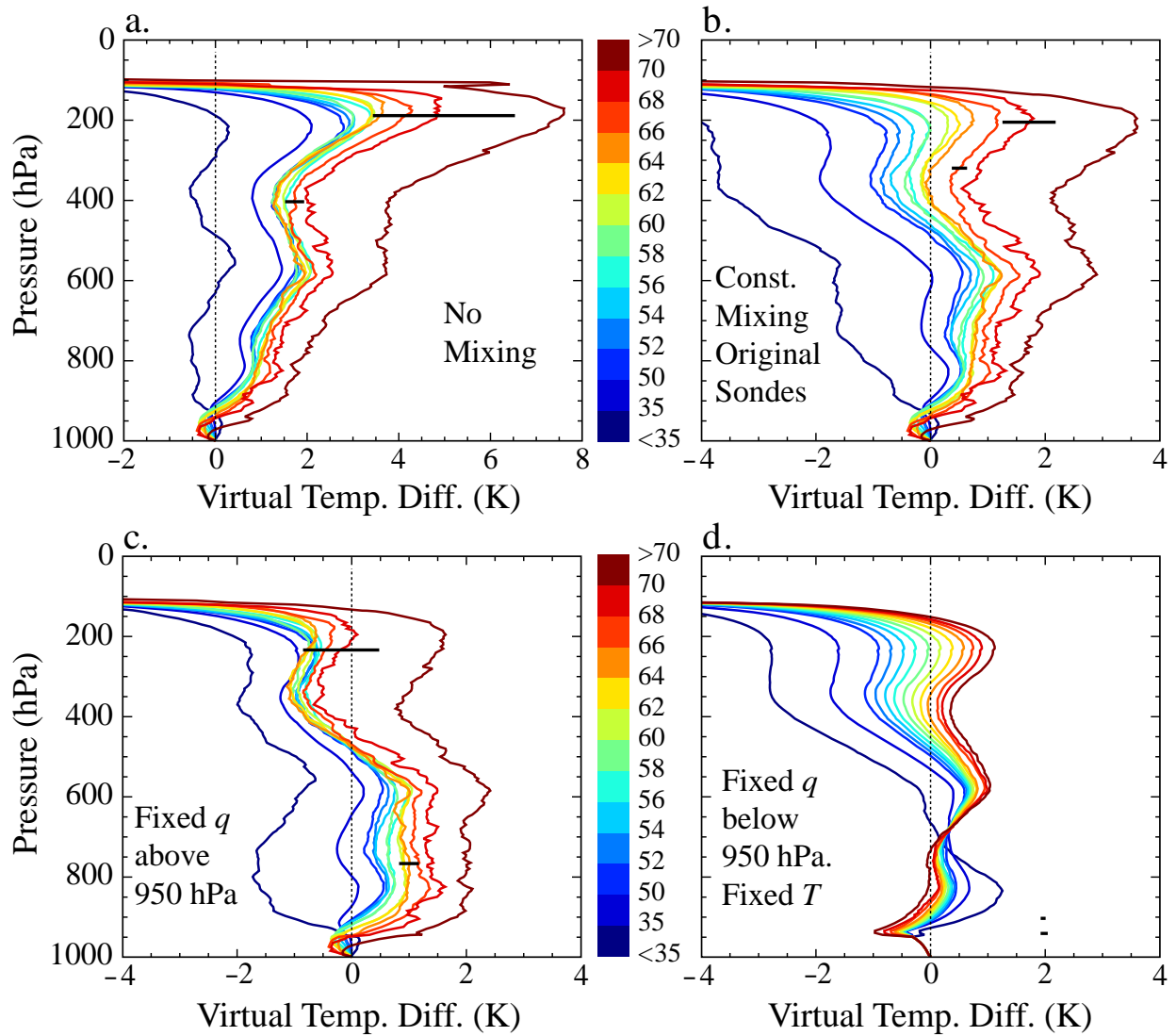


FIG. 7. Virtual temperature (K) difference profiles conditionally averaged on initial sonde column water vapor in mm (color bar), where the environmental (initial) sonde virtual temperature is subtracted from a profile determined by lifting a 1000-hPa parcel conserving total water and liquid equivalent potential temperature but also including: (a) no environmental mixing; (b) constant 0.5% mixing; (c) mixing with adjusted sonde profiles using mean specific humidity for levels above 950 hPa; (d) mixing with an adjusted sonde profile using mean temperature for all levels and mean specific humidity for levels below 950 hPa. Horizontal bars indicate limits of the maximum, as well as a representative, standard error range below 150 hPa (note that these bars appear on the side in panel (d) for visual clarity). For a few sondes in (c) and (d),  $q$  values have been slightly reduced at a few levels to remove supersaturation.

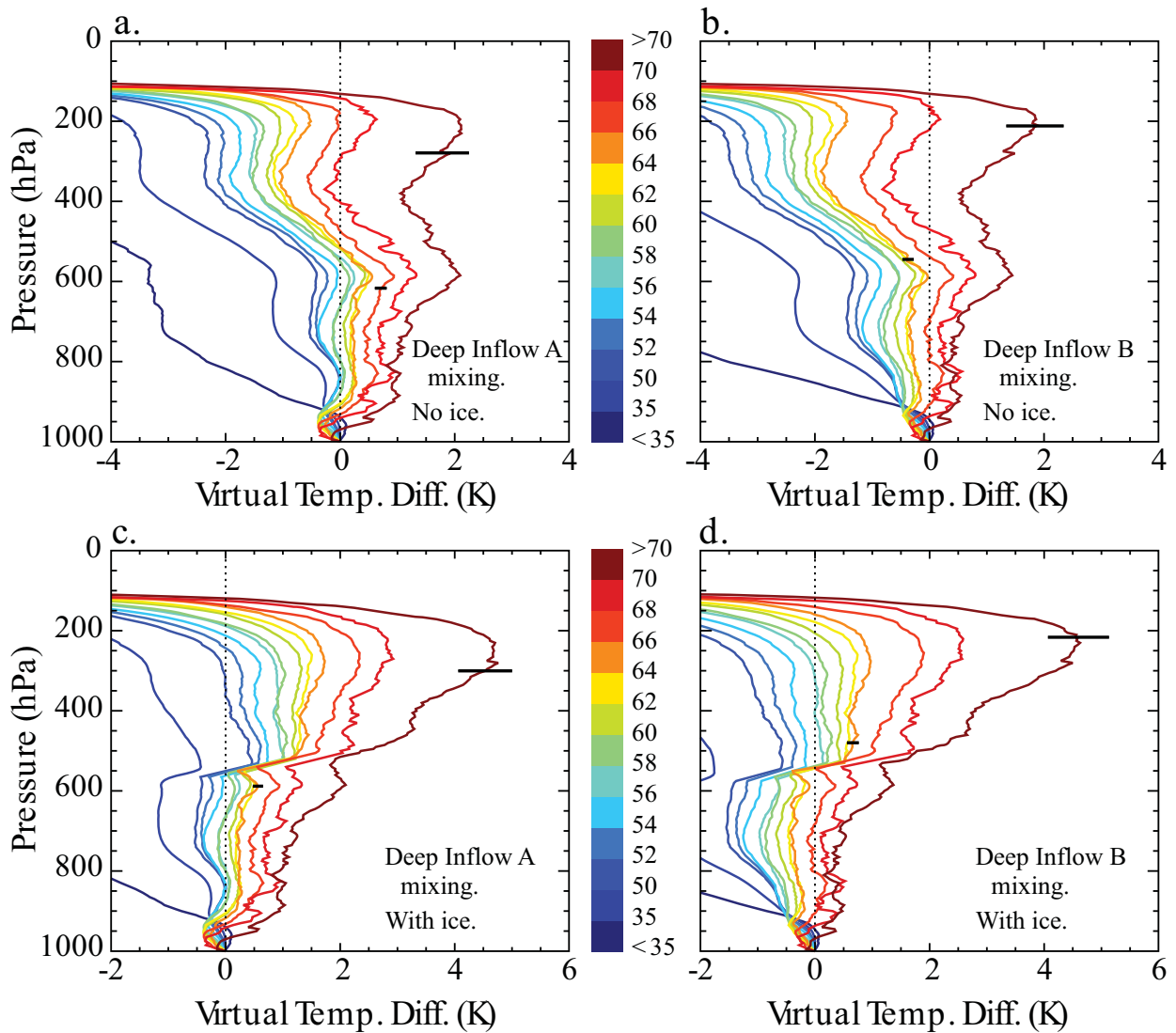


FIG. 8. Virtual temperature (K) difference profiles conditionally averaged on initial sonde column water vapor in mm (color bar), where the environmental (initial) sonde virtual temperature is subtracted from a profile determined by lifting a 1000-hPa parcel conserving total water and liquid equivalent potential temperature but also including: (a) Deep Inflow A mixing; (b) Deep Inflow B mixing; (c) Deep Inflow A mixing with conversion of liquid to ice, and following an ice-vapor reversible adiabat, above the freezing layer; (d) same as (c), but for Deep Inflow B mixing. In (c) and (d), the jumps in virtual temperature difference at the freezing level for all but the 1 uppermost and 2 lowermost column water vapor bins have been extended from about 10–15 hPa to 30 hPa, with a straight line connecting the otherwise original upper and lower curves, for visual clarity. Horizontal bars indicate limits of the maximum, as well as a representative, standard error range below 150 hPa.